On the June 21 and 25, 2015 CMEs interaction results on Earth's ionosphere and magnetosphere

Somaiyeh Sabri[1] and Stefaan Poedts[2,3]

[1]Institute of Geophysics, Faculty of Physics, University of Tehran, Tehran, Iran
[2]Centre for mathematical Plasma Astrophysics, Department of Mathematics, KU Leuven, Celestijnenlaan 200B, 3001 Leuven, Belgium
[3]Institute of Physics, University of Maria Curie-Skłodowska, ul. Radziszewskiego 10, PL-20-031 Lublin, Poland

Correspondence: Somaiyeh Sabri (s.sabri@ut.ac.ir)

Abstract. **Using a coupled EUHFORIA–Gorgon-Space modelling chain, we simulate the magnetosphere–ionosphere coupled response to two coronal mass ejections (CMEs) that impacted Earth on 23 and 28 June 2015. The first CME (CME1), launched on 21 June, triggered a major geomagnetic storm (Kp = 8), driving strong magnetosphere–ionosphere coupling characterized by a cross-polar cap potential of 160 kV and intense field-aligned currents exceeding 23 MA, key indicators of energy transfer from the solar wind into the high-latitude ionosphere. In contrast, the faster CME2 (launched on 25 June) produced only a weak disturbance (Kp ≈ 2) due to the absence of a prolonged southward interplanetary magnetic field (IMF), resulting in minimal magnetospheric driving and ionospheric feedback. These results validate an end-to-end space-weather forecasting framework and demonstrate that CME geoeffectiveness is governed primarily by the IMF orientation and reconnection-driven magnetosphere–ionosphere energy coupling, rather than by kinematic properties such as speed alone.** Using a coupled EUHFORIA–Gorgon-Space modelling chain, we simulate the magnetosphere–ionosphere coupled response to two coronal mass ejections (CMEs) that impacted Earth on 23 and 28 June 2015. The first CME (CME1), launched on June 21, triggered a major geomagnetic storm (Kp = 8), driving strong magnetosphere–ionosphere coupling characterised by a cross-polar cap potential of 160 kV and intense field-aligned currents exceeding 23 MA, key indicators of energy transfer from the solar wind into the high-latitude ionosphere. In contrast, the faster CME2 (launched on June 25) produced only a weak disturbance (Kp ≈ 2) due to the absence of a prolonged southward interplanetary magnetic field (IMF), resulting in minimal magnetospheric driving and ionospheric feedback. These results validate an end-to-end space-weather forecasting framework and demonstrate that CME geoeffectiveness is governed primarily by the IMF orientation and reconnection-driven magnetosphere–ionosphere energy coupling, rather than by kinematic properties such as speed alone.

1 Introduction

Coronal Mass Ejections (CMEs) are a primary source driver of major geomagnetic storms , representing and represent one of the most significant space weather space-weather threats to technological systems (Gosling, (1993); Lyon, (2000)). The severity of these storms is determined by the distinct properties of the CME-driven solar wind, which often

exhibits a significantly enhanced charged-particle density and a strongly southward-oriented interplanetary magnetic field (IMF). The interaction of this structured plasma with Earth's magnetosphere does not merely cause compression; it also drives a large-scale transfer of energy and momentum. This forces the magnetosphere into a disturbed state and enables energetic particles to penetrate deeply, ultimately funnelling energy into the ionosphere and triggering a complex chain of electrodynamic phenomena (Moore et al., (1999)).

The scientific community acknowledges the growing importance of space weather~~due to~~ , given its effects on human activities. Predicting space weather phenomena requires modelling distinct plasma environments, from the solar corona to the Earth's magnetosphere, each dominated by different physical processes (e.g., magnetohydrodynamics, kinetic theory). To address this issue, the ESA Virtual Space Weather Modelling Centre (VSWMC) has enhanced its capabilities to incorporate multiple models to predict space weather Poedts et al., (2020).

Transient structures in the solar wind, such as coronal mass ejections (CMEs) and corotating interaction regions, ~~play a vital role in causing space weather~~ drive space-weather effects ~~due to~~ through their ~~interaction~~ interactions with ~~the~~ Earth's coupled ~~magnetosphere-ionosphere~~ magnetosphere–ionosphere system. These transients often ~~exhibit strong southward magnetic-field components and can~~ carry interplanetary shocks at their leading edges and exhibit strong southward magnetic-field components. ~~When such a shock arrives, it~~ Shock impact causes a sudden increase in ~~the~~ solar wind dynamic pressure~~. This enhancement directly~~ , which rapidly compresses the dayside magnetopause ~~, a phenomenon known as a dynamic pressure enhancement (DPE)~~and the entire magnetospheric cavity. ~~The~~ This impulsive compression produces a characteristic ground magnetic signature~~of this rapid magnetospheric compression is~~ , a sharp ~~,~~ bipolar variation in the horizontal ~~magnetic field (Smith et al., (2019)). This phenomenon is generally referred to~~ component, known as a Sudden Impulse (SI) Smith et al., (2019). ~~In cases where this~~ When the initial compression is followed by sustained energy input (typically via southward IMF-driven reconnection) and the development of a full geomagnetic storm, the event is ~~more~~ specifically ~~called~~ termed a Storm Sudden Commencement (SC) ~~(Araki, (1994); Joselyn, (1990))~~Araki, (1994); Joselyn, (1990). Both SIs and SCs ~~are becoming more acknowledged as potential dangers~~ pose significant hazards to power ~~systems because they~~ infrastructure, as their rapid magnetic field variations can ~~generate~~ induce extremely high ~~levels of~~ geomagnetically induced currents (~~Eastwood et al., (2018)~~ GICs) in long conductors Eastwood et al., (2018).

Space weather, driven by solar activity such as Coronal Mass Ejections (CMEs), poses a significant risk to modern technological infrastructure. CMEs, which involve the violent expulsion of plasma and magnetic fields from the Sun, can trigger severe geomagnetic storms upon interaction with Earth's magnetosphere. The ionospheric response to CMEs can vary, depending on the properties of the CME and the geomagnetic conditions. The redistribution of ionospheric plasma during a geomagnetic storm can cause significant disruptions to radio communications. These disruptions can affect the reliability and quality of signal propagation through the ionosphere, thereby impacting various communication systems that rely on this medium (Kappenman, (2001); Astafyeva et al., (2014)). High-frequency (HF) radio signals can be more strongly absorbed in the ionosphere during such disturbances, thereby affecting long-distance radio communications by altering the propagation path and velocity of radio waves (Priyadarshi et al., (2016); Hayes et

al., (2017)). Additionally, radio signals can experience greater signal fading and path fluctuations as they traverse the ionospheric regions Araki, (1974). CME-induced ionospheric disturbances can also affect satellite-based navigation systems like GPS (Global Positioning System) (Demyanov et al., (2012)). The radio signals from GPS satellites passing through the disturbed ionosphere may experience propagation delays and errors (Rama Rao et al., (2009)). These delays can introduce inaccuracies in GPS position estimates, thereby affecting navigation and timing applications.

Furthermore, the super-magnetosonic solar wind ~~flow~~ flows past the magnetosphere~~leads to the formation of~~, forming a bow shock. The ever-changing nature of the solar wind causes the magnetospheric boundaries to shift continuously in response to variations in dynamic pressure and the interplanetary magnetic field (IMF). The size and shape of the magnetospheric obstacle primarily determine the stand-off distance of the bow shock. Since the magnetopause's location is ~~set~~ determined by the balance between solar wind dynamic pressure and ~~the~~ Earth's magnetic pressure, the bow shock's position ~~exhibits~~ shows a clear dependence on solar wind conditions. Empirical models often ~~parameterize~~ parameterise the bow shock based on this relationship (Merka et al., (2005); Peredo et al., (1995)), building on the foundational gasdynamic principles established by Spreiter et al., (1966).

Beyond usual solar wind fluctuations, the most rapid and substantial movements of magnetospheric boundaries are caused by distinct transient structures, particularly interplanetary shocks (Dryer et al., (1967); Grib et al., (1979)). Numerical simulations and spacecraft observations have consistently shown that the impact of an interplanetary shock on the magnetosphere leads to a global, rapid compression. For instance, simulations by Samsonov et al., (2010) demonstrate significant inward motion of the bow shock and magnetopause upon the shock's arrival. This compression ~~is a direct driver of~~ directly drives ground-level phenomena such as Sudden Commencements (SCs). Intriguingly, these model results are strongly supported by in-situ spacecraft measurements (Pallocchia, (2013)).

In general, empirical models have limitations in capturing the motion of shocks that arise in response to rapid changes in the upstream solar wind. Specifically, there is limited understanding of when these statistical models become unsuitable, and ~~it is not evident how these models deviate from reality during the dynamic transition of boundaries towards new equilibrium states.~~ it is unclear how they deviate from reality during the dynamic transition of boundaries toward new equilibrium states. To overcome these limitations, the space science community has long employed global magnetohydrodynamic (MHD) simulations, a powerful tool for modelling the coupled system in a self-consistent manner. Since their development in the 1990s (e.g., Ogino, (1994); Raeder, (1995)), global MHD models have been extensively used to study magnetospheric dynamics. Today, a suite of well-established models (e.g., the LFM code, the OpenGGCM, SWMF/BATS-R-US) continues to advance our understanding. Within this modelling paradigm, our study employs the Gorgon code to conduct global MHD simulations of Earth's magnetosphere under dynamic solar wind conditions (Chittenden et al., (2004); Ciardi et al., (2007); Mejnertsen et al., (2016)).

While empirical models provide valuable statistical representations of magnetospheric boundaries, they are inherently limited in capturing the rapid, non-equilibrium dynamics driven by transient solar wind structures~~like~~, such as CME-driven shocks. These models struggle to accurately represent the motion of shocks and the transient reconfiguration of boundaries, such as the bow shock and magnetopause, during their dynamic transition to new equi-

librium states. To overcome these limitations, this study employs the Gorgon-Space code, a global magnetohydrodynamic (MHD) model. The primary aim of using Gorgon-Space is to conduct high-fidelity, time-dependent simulations of Earth's magnetosphere-ionosphere system in response to realistic, time-varying solar wind input. This approach allows us to accurately capture the full system's consistent and coupled response, including magnetospheric compression, the activation of current systems, and the subsequent ionospheric electrodynamic feedback, thereby providing a physically consistent framework to investigate the geospace environment's response to specific CME events (Chittenden et al., (2004); Ciardi et al., (2007); Mejnertsen et al., (2016)).

The coupling ~~between~~ among the solar wind, magnetosphere, and ionosphere, mediated by field-aligned currents (FACs), is a fundamental driver of ~~space weather~~ space-weather phenomena. Accurate global MHD modelling of this coupled system is therefore essential for prediction (e.g., Pulkkinen, (2007); Gombosi et al., (2021)).

Significant progress has been made in simulating large-scale magnetospheric dynamics and their ionospheric signatures. Models ~~like~~ such as the Space Weather ~~Modeling~~ Modelling Framework (SWMF) and the Gorgon-Space code have demonstrated skill in reproducing global convection patterns and regional FAC distributions during specific events (e.g.,Wiltberger et al., (2017); Sorathia et al., (2022)). These models solve the coupled MHD magnetosphere-ionosphere system, in which ionospheric conductances, critical for determining the electric field mapped to the magnetosphere, are often derived from empirical relations.

The remaining challenge, however, lies in ~~the accurate quantitative reproduction of~~ accurately reproducing electric fields and current densities in key regions~~like~~, such as the plasma sheet, during dynamic solar wind driving. Discrepancies between modelled and observed fields in these regions can propagate~~to affect~~, affecting the entire system's response ~~,~~ and impacting the fidelity of space weather forecasts. This study specifically addresses this challenge by evaluating the performance of the Gorgon-Space code in simulating FACs and associated electric fields. We focus on the role of the inner boundary definition and the empirical conductance models in determining the accuracy of the coupled solution.

In the Gorgon-Space code, the ionosphere is treated as a two-dimensional spherical shell at approximately 1 R_E (Earth radius) from the Earth's ~~center~~centre. This boundary is ~~characterized~~ characterised by a height-integrated conductance model (typically including both Pedersen and Hall conductances), which may be specified as empirical values or calculated self-consistently based on precipitation patterns. The magnetosphere-ionosphere coupling is enforced by mapping field-aligned currents (FACs), calculated from the magnetospheric vorticity in the simulation, down to this ionospheric shell. The ionospheric solver then ~~calculates~~ computes the resulting electric potentials and currents, which, in turn, influence the magnetospheric flow via boundary conditions on the magnetic field and plasma, thereby closing the coupled system.

The upstream (sunward) boundary of the simulation is driven by time-dependent solar wind parameters obtained from the EUHFORIA (European Heliospheric Forecasting Information Asset) model. These parameters, which include number density, velocity, thermal pressure, and the interplanetary magnetic field (IMF) components, provide the external forcing for the magnetospheric simulation.

The dynamic and non-uniform nature of Earth's magnetosphere presents a substantial modelling challenge, as a complex interplay between the solar wind, internal magnetic field, and various plasma populations determines its global state. A comprehensive understanding requires modelling the magnetosphere and ionosphere as a tightly coupled system in which energy and momentum are transferred along magnetic field lines. This magnetosphere-ionosphere (M-I) coupling is primarily mediated by Field-Aligned Currents (FACs), which are intrinsically linked to vorticity and pressure gradients in the magnetospheric plasma. The Gorgon-Space code is uniquely well-suited to model this coupled system, as it solves the global MHD equations to self-consistently simulate the vast magnetospheric domain while simultaneously capturing FAC generation and their closure in the ionosphere. Consequently, this study ~~utilizes~~ utilises Gorgon-Space to investigate the transient variations in FACs and ionospheric potentials driven by CME impacts, providing a physics-based assessment of the dynamic M-I system's response to extreme space weather events.

This study applies the established end-to-end modelling approach, linking heliospheric and magnetospheric codes, to the specific case of interacting CMEs in June 2015, using the EUHFORIA–Gorgon-Space coupling. Gorgon-Space was selected for this work due to its unique formulation based on the magnetic vector potential, which inherently preserves $\nabla \cdot \mathrm{B} = 0$ to machine precision. This property is critical for maintaining numerical stability during extreme, rapidly varying compression events, such as CME impacts, where spurious magnetic monopoles in standard B-field solvers can degrade solution fidelity. Furthermore, Gorgon-Space has been rigorously validated for simulating field-aligned currents (FACs) and ionosphere-magnetosphere coupling during storm-time conditions Mejnertsen et al., (2018); Eggington et al., (2020). Leveraging these strengths, we conduct a comparative analysis of two CME events and successfully capture intense geoeffective signatures, including FACs exceeding 23 million amperes and a cross-polar cap potential of $\sim$160 kV for CME1, while correctly reproducing the muted response to CME2. These results demonstrate Gorgon-Space's capability to forecast key magnetospheric drivers of space weather impacts, providing a validated, physics-based methodology for translating heliospheric CME forecasts into quantifiable geospace impact predictions.

The objective of our study is to investigate the interaction between two CMEs and Earth and their effects on Earth's ionosphere and magnetosphere. In this research, we ~~utilize~~ utilise Gorgon-Space to explore how Earth's magnetosphere ~~reacts to the interaction~~ responds to interactions with CMEs and to study the impact of CMEs on the magnetosphere. In conclusion, the study examines how the ionosphere reacts to the interaction between CMEs and the magnetosphere. It also evaluates the consequential effects on the ionosphere, including induced current densities, which ~~have significant impacts on~~ significantly affect communication and space weather.

2 Method

~~**Gorgon is a 3D magnetohydrodynamic code, initially developed for studying high-energy, collisional plasma interactions such as Z-pinches (Chittenden et al., (2004); Jennings et al., (2010)), laser-plasma interactions (Smith et al., (2007)), and magnetic tower jets Ciardi et al., (2007). It has recently been adapted to simulate planetary magnetospheres and their interaction with the solar wind (Mejnertsen et al., (2016)). The code solves the resistive MHD equations using**~~

a semiconservative formulation. In this approach, the equations for mass, momentum, and energy are solved in a fully conservative form, which ensures accurate capture of shocks and discontinuities. The magnetic field, however, is evolved using the induction equation (a non-conservative form), typically coupled with a divergence-cleaning technique to maintain the solenoidal constraint ($\nabla \cdot \mathrm{B} = 0$). Most of its primary features are designed for intricate collisional and resistive Magnetohydrodynamics (MHD) phenomena Ciardi et al., (2007).

2.1 EUHFORIA Heliospheric Model

Gorgon-Space has been created specifically to tackle the challenge of conducting global magnetospheric simulations for space weather and space physics. Therefore, it currently represents The European Heliospheric Forecasting Information Asset (EUHFORIA) is a distinct area three-dimensional magnetohydrodynamic (MHD) model of enhancement and has been optimized and evaluated for particular use cases. A key feature of Gorgon-Space is the inner heliosphere that it evolves simulates the magnetic vector potential (A) instead propagation of solar wind structures from the magnetic field (B) directlySun to 2 AU Pomoell & Poedts, (2018); Rodgers-Lee et al. (2021). This approachThe model domain extends from a spherical inner boundary at 0.1 AU to an outer boundary at 2.0 AU, also used in other models (e.g., Yagi et al., (2009)), inherently guarantees that with spatial resolution increasing with heliocentric distance. EUHFORIA solves the ideal MHD equations for a fully ionised plasma under the influence of solar gravity and the interplanetary magnetic fieldremains divergence-free (i.e., $\nabla \cdot B = 0$) by construction, which is a significant numerical advantage (Mejnertsen et al., (2018); Eggington et al., (2020)).

Coronal Mass Ejections are injected at the inner boundary as time-dependent, flux-rope structures characterised by their launch time, location (longitude/latitude), angular width, and initial speed. The model self-consistently propagates these transients through the ambient solar wind, capturing CME–CME and CME–solar wind interactions, shock formation, and magnetic field evolution en route to Earth.

At the L1 Lagrange point (approximately 1.5 million km sunward of Earth), EUHFORIA provides time series of key solar wind parameters: proton number density n_p (cm^{-3}), bulk velocity V (km s^{-1}), thermal pressure P_{th} (nPa), and the three components of the interplanetary magnetic field B (nT) in GSE coordinates. These parameters serve as the direct upstream boundary conditions for global magnetospheric models such as Gorgon-Space.

2.2 Gorgon-Space Model

Gorgon is a 3D magnetohydrodynamic code, originally developed to study high-energy, collisional plasma interactions, such as Z-pinches (Chittenden et al., (2004); Jennings et al., (2010)), laser-plasma interactions (Smith et al., (2007)), and magnetic tower jets Ciardi et al., (2007). It has recently been adapted to simulate planetary magnetospheres and their interaction with the solar wind (Mejnertsen et al., (2016)). The code solves the resistive MHD equations using a semiconservative formulation. In this approach, the equations for mass, momentum, and energy are solved in a fully conservative form, which ensures accurate capture of shocks and discontinuities. The magnetic field, however, is evolved using the induction equation (a non-conservative form), typically coupled with a divergence-cleaning technique

to maintain the solenoidal constraint ($\nabla \cdot \mathrm{B} = 0$). Most of its primary features are designed for intricate collisional and resistive Magnetohydrodynamics (MHD) phenomena Ciardi et al., (2007).

Gorgon-Space has been created specifically to tackle the challenge of conducting global magnetospheric simulations for space weather and space physics. Therefore, it currently represents a distinct area of enhancement and has been optimised and evaluated for particular use cases. A key feature of Gorgon-Space is that it evolves the magnetic vector potential (A) instead of the magnetic field (B) directly. This approach, also used in other models (e.g., Yagi et al., (2009)), inherently guarantees that the magnetic field remains divergence-free (i.e., $\nabla \cdot B = 0$) by construction, which is a significant numerical advantage (Mejnertsen et al., (2018); Eggington et al., (2020)).

Gorgon-Space ~~utilizes~~ utilises a definite-sized 3D Cartesian grid to solve the MHD equations. Moreover, Gorgon possesses a highly advanced capability to scale linearly and in parallel ~~to~~ across numerous cores, ~~based on~~ using fully explicit numerical methods. It found the impact of the solar wind on several important parameters in the tail, including the magnetic field, field-aligned current, plasma velocity, and plasma pressure. These global quantities depend on the magnetosphere's large-scale equilibrium, which is believed to be accurately described by magnetohydrodynamics (MHD).

Gorgon uses a fully explicit Eulerian formulation of the resistive semiconservative MHD equations for a fully ~~ionized~~ ionised plasma as

$$\frac{\partial \rho}{\partial t} + \nabla \cdot (\rho \mathbf{V}) = 0, \tag{1}$$

$$\rho \left[\frac{\partial \mathbf{V}}{\partial t} + (\mathbf{V} \cdot \nabla)\mathbf{V} \right] = \left(\frac{1}{\mu} \nabla \times \mathbf{B} \right) \times \mathbf{B} - \nabla (P_e + P_p), \tag{2}$$

$$\frac{\partial \mathbf{B}}{\partial t} = \nabla \times (\mathbf{V} \times \mathbf{B}) + \eta \nabla^2 \mathbf{B}, \tag{3}$$

$$\frac{\partial \epsilon_p}{\partial t} + \nabla \cdot (\epsilon_p \mathbf{V}) = -P_p \nabla \cdot (\mathbf{V}) - \Delta_{pe}, \tag{4}$$

$$\frac{\partial \epsilon_e}{\partial t} + \nabla \cdot (\epsilon_e \mathbf{V}) = -P_e \nabla \cdot (\mathbf{V}) + \Delta_{pe} - \Lambda + \eta |\mathbf{J}^2|, \tag{5}$$

The plasma density, plasma velocity, magnetic field, proton internal energy density, electron internal energy density and thermal plasma pressure are represented by the variables ρ, $\mathbf{V}$, $\mathbf{B}$ ϵ_p, ϵ_e, and P respectively. The values μ, η, and $\gamma = 5/3$ represent the magnetic permeability, the magnetic diffusivity, and the ratio of specific heats at constant pressure and volume, respectively. The permeability of vacuum is considered i.e. $\mu = 4\pi \times 10^{-7}$ Hm^{-1}. The deBar correction, known as Von Neumann artificial viscosity, is ~~utilized to properly~~ utilised to accurately detect and enhance ~~the conservation of energy during~~

energy conservation in the presence of shocks (Benson, (1992)). Gorgon makes use of second-order Van Leer advection to solve the advection terms in equations. It also employs a variable time step, which automatically satisfies the relevant Courant conditions.

The MHD formulation in Gorgon has its roots in ~~high-energy density~~ high-energy-density plasma physics, leading to several features that are atypical ~~for~~ of global magnetospheric simulations. A key aspect is that it solves separate internal energy equations for electrons and protons, allowing them to be out of thermodynamic equilibrium. The electron energy equation includes physically important terms.

Ohmic Heating ($\eta|\mathbf{J}^2|$), where the resistivity η is treated as a constant value or a Spitzer-like model dependent on local electron temperature Jennings et al., (2010). Electron-Proton Energy Exchange (Δ_{pe}), which is modelled as a collisional relaxation term of the form $\Delta_{pe} = \nu_{ep} nk(T_p - T_e)$, driving the two populations towards thermal equilibrium (Chittenden et al., (2004)). Given the tenuous plasma conditions in the magnetosphere, the optically thin radiation loss term (~~$varLambda$~~Λ) is neglected in the present study ($\Lambda = 0$) ~~, as~~ because radiative cooling is negligible relative to other energy transport mechanisms.

Furthermore, the code evolves internal energy rather than total energy. While this means total energy is not strictly conserved, it is a deliberate design choice that significantly enhances numerical robustness. This approach effectively mitigates the occurrence of non-physical negative pressures in regions of high magnetic energy or strong shocks, which is a common numerical challenge in conservative total-energy schemes.

The Gorgon-Space code solves separate internal energy equations for electrons and protons. Therefore, the total thermal pressure provided by EUHFORIA must be partitioned at the boundary. For this study, we assume the proton and electron populations are in thermal equilibrium ($T_p = T_e$) upon entry, resulting in an equal split of the pressure ($P_p = P_e = P_{tot}/2$). The upstream (sunward) boundary of the simulation is driven by time-dependent solar wind parameters obtained from the EUHFORIA heliospheric model.

The treatment of the inner boundary of the magnetospheric domain in Gorgon is similar to that used in other codes, which are coupled to a thin-shell ionosphere model. The approach is to define the plasma density, temperature, and velocity ~~everywhere within~~ throughout the spherical region enclosed by the inner boundary and ~~to~~ enforce ~~these~~ them at every time step. The cells for which this is performed are flagged as inner boundary cells if the cell centre lies within the specified inner boundary radius RIB, typically set to 4 RE (Earth radius). Whilst the MHD equations are not solved in this region, the cells just outside of the boundary are updated based on the inner boundary properties. Thus, the cold, dense plasma expands to form a plasmasphere, and the inner boundary flow feeds into the global magnetosphere.

The grid namelist specifies the domain size and resolution~~of the grid~~, as well as ~~setting~~ the dimensional splitting for ~~the~~ parallelisation. The default box has dimensions 90 x 80 x 80 RE and spans (X, Y, Z) = ([-24,66], [-40,40], [-40,40]) RE, and should be kept as close as possible to these dimensions ~~as possible~~ to balance runtime and stability. The simulation utilizes a fixed computational grid with a resolution of 0.5 R_E to resolve the global structure of the magnetosphere. This resolution was chosen to accurately capture large-scale boundaries and dynamics, such as the positions of the bow

Time at 21.5R	Longitude(deg)	Latitude(deg)	Half Angle(deg)	Speed(km/s)
2015-06-010T00:05:00Z	-31	30	43	853
2015-06-014T08:47:00Z	40	-23	36	701
2015-06-016T10:53:00Z	25	-50	39	570
2015-06-18T20:00:00Z	-50	11	45	1000
2015-06-19T14:59:00Z	9	-33	54	603
2015-06-21T05:01:00Z	-8	7	47	1250*
2015-06-22T21:10:00Z	3	14	45	1155
2015-06-25T10:51:00Z	46	23	41	1450**

Table 1. List of ~~the~~ CMEs observed during 10–25 June 2015 and injected into EUHFORIA. Events marked with * (21 June) and ** (25 June) correspond to CME1 and CME2, respectively, the two events selected for detailed magnetospheric simulation with Gorgon-Space due to their ~~characteristics~~ contrasting geoeffectiveness.

shock and magnetopause, and the overall evolution of the magnetotail, while remaining computationally tractable for the extended simulation runs required for this study. The grid dimensions are (n_x, n_y, n_z) = (180, 160, 160) cells, which defines the 0.5 R_E grid spacing throughout the domain.

The simulation ~~utilizes~~ utilises a fixed computational grid within a Cartesian domain spanning from (X, Y, Z) = ([-24,66], [-40,40],[-40,40]) R_E. This domain size encompasses the critical regions from the dayside bow shock to a significant portion of the magnetotail. The grid consists of (n_x, n_y, n_z) = (180, 160, 160) cells, resulting in a uniform resolution of 0.5 R_E. This resolution was chosen to accurately capture large-scale boundaries and dynamics, such as the positions of the bow shock and magnetopause and the general evolution of the magnetotail, while maintaining computational tractability for the parameter study.

3 Numerical results and discussion

We selected two CMEs from the June 2015 campaign that exhibited contrasting geoeffectiveness despite both being fast events:

- **CME1: Launched on 21 June 2015 at 05:01 UT from heliographic coordinates (longitude = –8°, latitude = +7°) with an initial speed of 1250 km s^{-1} (Table 1). EUHFORIA predicted its arrival at Earth on 23 June 2015 at 00:03 UT, where it triggered a major geomagnetic storm (peak Kp = 8).**

- **CME2: Launched on 25 June 2015 at 10:51 UT (longitude = +46°, latitude = +23°) with a higher initial speed of 1450 km s^{-1}. EUHFORIA predicted its arrival on 28 June 2015 at 12:52 UT, but it produced only a minor disturbance (peak Kp $\approx$ 2).**

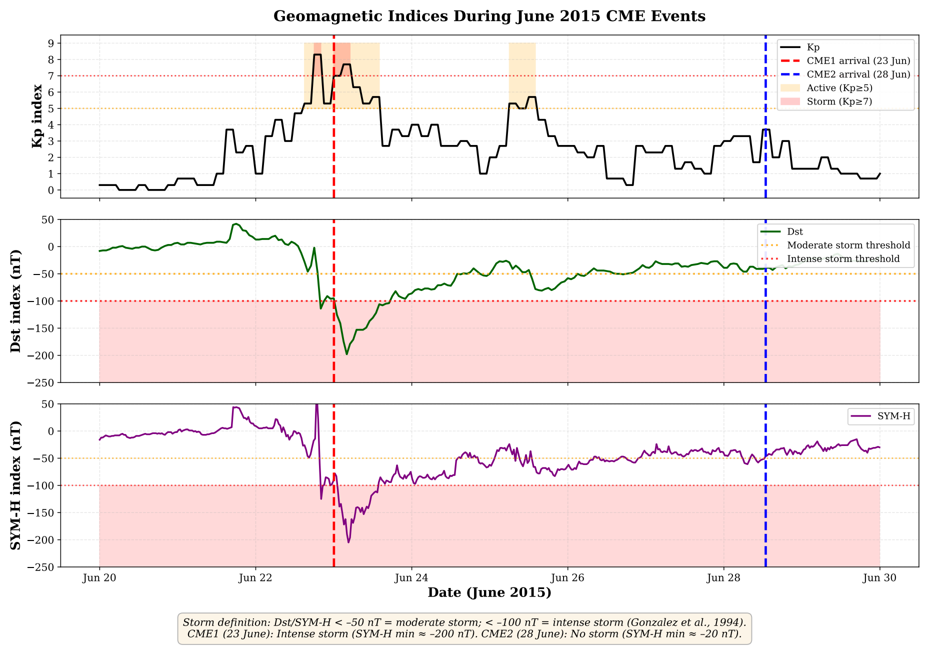

Figure 1. Geomagnetic response to CME1 (23 June 2015) and CME2 (28 June 2015) impacts. Top to bottom: Kp index~~calculated~~ , Dst index, and SYM-H index. Vertical dashed lines mark EUHFORIA-predicted CME arrival times at L1. Storm intensity thresholds are indicated by horizontal lines: orange (-50 nT, moderate storm) and red (-100 nT, intense storm) per Gonzalez et al. (1994). CME1 produced an intense geomagnetic storm with SYM-H minimum ≈ -200 nT, while CME2 showed only a minor disturbance (SYM-H minimum ≈ -20 nT) despite a brief Kp elevation. This demonstrates that high Kp values alone do not constitute a magnetic storm; Dst/SYM-H quantifies the ~~EUHFORIA~~development of the ring current that defines storm intensity.

This pair provides an ideal test case to isolate the role of IMF orientation versus CME kinematics in determining geoeffectiveness.

~~The K—index quantifies disturbances in the Earth's magnetic field in the horizontal orientation and is classified with a numerical score ranging from 0 to 9. In peaceful conditions, the Kp value is approximately 1. However, during severe geomagnetic storms, it is about 9. The Kp index is a global evaluation of the K index, based on information collected from ground-based magnetometers (Bartels & Veldkamp, (1949)). When it comes to the actual situation, Kp acts as an exceptional indicator for any anomalies in the Earth's magnetic field. Currently, Kp is important as it measures the amount of energy transferred from the solar wind to Earth. It is used by space weather services almost immediately.~~ **While CME2 exhibited higher kinematic speed (1450 km/s vs. 1250 km/s for CME1), its geoeffectiveness was minimal due to the absence of sustained southward IMF (Bz > -5 nT for >90% of the event duration). This contrasts sharply with CME1, which maintained Bz < -15 nT for >6 hours, driving intense dayside reconnection (Ey > 15 mV/m) and producing the observed G4 storm (Kp=8, Dst≈-200 nT). These results definitively demonstrate that CME speed alone is insufficient to predict storm intensity — the orientation of the embedded magnetic field governs geoeffectiveness.**

~~In our earlier research, we examined~~ Geomagnetic activity indices provide complementary diagnostics for characterising the ~~propagation~~ intensity and physical drivers of ~~eight coronal mass ejections (CMEs) from June 10-25, 2015 (table 1; Sabri & Poedts, (2025)). To investigate geoeffectiveness, we selected two~~ space weather events~~that represented contrasting outcomes~~. ~~To objectively classify the global geomagnetic impact of these events, we used the~~ The Kp index (~~Fig. 1~~planetary K-index) quantifies global auroral-zone magnetic disturbances on a quasi-logarithmic scale from 0–9, derived from 3-hourly measurements at 13 mid-latitude magnetometers Bartels & Veldkamp, (1949). While ~~the~~ Kp ~~index~~ is ~~a 3-hourly measure~~operationally valuable for space-weather alerts because of its sensitivity to high-latitude currents and substorm activity, it ~~serves as a robust, global standard for identifying~~ does not directly measure the ~~overall severity of a geomagnetic~~ ring current responsible for main-phase storm ~~(Bartels & Veldkamp, (1949))~~development.

~~This clear dichotomy in global impact~~ inner magnetosphere and is therefore the ~~central motivation~~ authoritative metric for ~~our simulation study. We do not use the Kp index to resolve short-period magnetospheric dynamics; instead, it defines the two extreme solar wind driving conditions we aim to model: a severe~~ assessing storm intensity.~~CME1~~For definitive storm classification, ~~launched on June 21st at 02:36 UT~~the Dst (Disturbance Storm Time) index Sugiura, (1964) and its 1-minute resolution counterpart SYM-H Iyemori, (1990) are the standard metrics. These indices, ~~arrived at~~ derived from low-latitude magnetometer networks, measure the depression of the horizontal magnetic field component caused by the symmetric ring current encircling Earth~~on June 23rd~~. ~~The Kp index reveals that this event drove~~ By convention Gonzalez et al., (1994), a ~~major~~ geomagnetic storm is defined when Dst/SYM-H $\leq$ -50 nT, with ~~values reaching a maximum~~ categories of ~~Kp=8~~ moderate (~~Fig. 1~~-50 > Dst $\geq$ -100 nT)~~. In stark contrast~~, ~~CME2~~ intense (~~launched June 25th~~-100 > Dst $\geq$ -250 nT)~~arrived on June 28th~~, and ~~resulted in only a minor perturbation~~super-intense (Dst < -250 nT) storms. Unlike Kp, ~~with~~ Dst/SYM-H directly reflects energy injection into the ~~Kp index remaining low at a peak of 2.~~

~~This clear dichotomy in global impact~~ inner magnetosphere and is therefore the ~~central motivation~~ authoritative metric for ~~our simulation study. We do not use the Kp index to resolve short-period magnetospheric dynamics; instead, it defines the two extreme solar wind driving conditions we aim to model: a severe~~ assessing storm intensity.

Dst and ~~a quiet period~~SYM-H values shown in Fig.~~Using~~ 1 are observational data from the ~~Gorgon Space MHD code~~OMNI databases, ~~we simulate the response~~ used here solely for event classification and validation of the ~~coupled magnetosphere-ionosphere system to these two fundamentally different scenarios. The simulations allow us to move beyond the global Kp metric and investigate the high-resolution~~simulated magnetospheric response, ~~local plasma parameters~~ not as model outputs. These indices objectively confirm that CME1 (~~e.g., pressure distributions and field-line topology~~23 June 2015) ~~that characterise a severe~~ produced an intense geomagnetic storm ~~versus a quiet time. This approach tests whether the EUHFORIA-predicted~~(SYM-H minimum $\approx$ -200 nT), ~~Kp-classified strong storm~~ while CME2 (~~CME1~~28 June 2015) ~~yields~~ generated only a ~~magnetospheric state significantly different from that of the weak event~~ minor disturbance (~~CME2~~SYM-H minimum $\approx$ -20 nT) ~~in the Gorgon-Space model~~despite a brief Kp elevation during its shock arrival.

~~Our global MHD simulation has focused on~~ While Sabri & Poedts, (2025) established the ~~large-scale magnetospheric response driven by CME1, particularly the reconnection-mediated energy transfer. It is important~~ fidelity of EUHFORIA's heliospheric forecasts and their conversion to ~~note that our model~~geomagnetic activity estimates, ~~while capturing~~ the ~~essential magnetohydrodynamics, does not address kinetic-scale phenomena~~ present work focuses on the next critical step in the ~~upstream regions. For instance, the interaction of the~~ space weather chain: translating EUHFORIA's time-dependent solar wind ~~with the bow shock forms the foreshock~~parameters (density, ~~where reflected particles generate waves and can undergo further acceleration Eastwood et al., (2005). These foreshock disturbances can subsequently interact with the magnetopause~~velocity, ~~potentially influencing local reconnection rates and wave activity. Future studies coupling global MHD models with kinetic treatments of the foreshock region could therefore provide~~ IMF) at L1 into a ~~more complete picture~~ self-consistent simulation of the ~~initial solar wind-magnetosphere interaction chain during extreme~~ coupled magnetosphere–ionosphere response using Gorgon-Space. We do not aim to improve Kp/Dst forecasting algorithms; rather, we leverage these indices solely to classify the two contrasting events ~~like~~ (major storm vs. weak disturbance) and then investigate, through first-principles MHD simulation, the ~~one studied here~~underlying plasma processes (magnetospheric compression, FAC intensification, convection electric fields) that produce these differing geomagnetic signatures. This end-to-end approach bridges heliospheric prediction and geospace impact quantification, providing a physics-based framework for operational space-weather forecasting.

3.1 Gorgon-Space

A systematic study was conducted to demonstrate the global fluctuations in the magnetic field using magnetic observations. These differences were credited to the influence of solar wind discontinuities on both the Earth's magnetosphere and ionosphere. Magnetic reconnection is the primary process through which plasma and energy from the solar wind are introduced into the magnetosphere. However, there are also cases where viscous-like effects can play a role, especially when the magnetic setup is unsuitable for reconnection. In this part, we examine how the arrival of CMEs affects Earth. The Gorgon-Space code is ~~utilized~~ utilised in this specific situation.

The configuration of the simulation domain is shown in Fig. 2. ~~When the solar wind interacts with the Earth's magnetosphere, it generates a bow shock wave that forms ahead of the magnetopause. This results in the creation of a turbulent region known as the magnetosheath situated between them, a structure first described in the seminal work of Spreiter et al., (1966) and studied in its turbulent nature by Lucek et al., (2005) and Burgess & Scholer, (2013).~~ When the solar wind interacts with the Earth's magnetosphere, it generates a bow shock wave that forms ahead of the magnetopause. This results in the formation of a turbulent region, known as the magnetosheath, situated between them, a structure first described in the seminal work of Spreiter et al., (1966) and studied in its turbulent nature by Lucek et al., (2005) and Burgess & Scholer, (2013). To enable plasma to move away from the planet, for example, when the solar wind is redirected around the magnetopause or when magnetospheric plasma is expelled towards the tail, it is necessary to implement free-flow at the outer boundaries of the simulation domain. One exception to this rule occurs

on the side of the box facing the ~~sun~~Sun, specifically on Earth's left side. This is where the simulation receives and relies on the solar wind inflow to serve as the main source of plasma.

The simulation domain of the Gorgon-Space MHD code (Fig. 2) is designed to model Earth's magnetosphere, with its sunward boundary positioned at the bow shock. The key input to the simulation is the time-dependent solar wind plasma, whose parameters are specified at this boundary. These parameters, derived from the EUHFORIA heliospheric model, illustrate variations in the solar wind that directly control the formation and properties of the bow shock. On the remaining outer boundaries (tailward, lateral, and polar), free-flow (outflow) conditions are implemented. This configuration allows plasma to exit the domain, whether it is solar wind being deflected around the magnetosphere or magnetospheric plasma being ejected downtail, without generating unphysical reflections, a standard approach in global magnetospheric simulations Spreiter et al., (1966); Lucek et al., (2005); Burgess & Scholer, (2013).

To allow the plasma to leave ~~the~~ Earth's vicinity, it is necessary to incorporate ~~free-flow~~ free flow outside the simulation area. In simpler terms, when the flow of charged particles from the ~~sun~~ Sun is directed away from the boundary of a magnetic field, the plasma in the magnetic field is expelled towards the ~~center~~centre. It should be acknowledged that on the left side of the Earth, there is a box with its sunny side facing towards the Sun. This box serves as the primary entry point for the solar wind, which provides the plasma in the simulation. The solar wind's force, speed, and magnetic field can be established for the incoming plasma and ~~analyzed for~~ analysed to determine its interaction with the ~~magnetic field of the planet.~~ planet's magnetic field.

Gorgon-Space was selected for this study due to its divergence-free magnetic field formulation (via vector potential evolution), which ensures numerical stability during extreme compression events, and its validated performance in simulating FACs and ionospheric coupling during CME impacts Mejnertsen et al., (2018); Eggington et al., (2020).

3.1.1 Magnetospheric Response

The magnetosphere is influenced by interactions with the solar wind, which can be either viscous or ~~pressure-related according to~~ pressure-driven, as described by Newell et al., (2008). The physical mechanisms that allow plasma and energy to flow from the solar wind into the magnetosphere are reconnection (Dryer, (1961)) and viscous interaction (Axford & Hines, (1961)). Dayside magnetic reconnection opens Earth's closed field lines, enabling direct entry of solar wind plasma and momentum into the magnetosphere via magnetic flux transport. The solar wind conditions driving this simulation are the direct output from the EUHFORIA heliospheric model at the Earth's location (L1 point) for the arrival of the first CME on June 23, 2015. This provides a physically consistent, time-dependent input boundary condition for the Gorgon-Space model, linking the CME's interplanetary propagation to its geoeffective impact.

~~Fig.~~Figure 3 shows the initial solar wind parameters used as input for the magnetospheric simulation, corresponding to the CME arrival time at Earth on June 23, 2015, at 00:03 UT. The panels display the three magnetic field components (in nT), the velocity components (in ~~km/s~~km/s), the number density (in ~~cm^{-3}~~cm^{-3}), and the temperature (in eV), as extracted from the EUHFORIA output at this specific time. The figure also indicates the spatial limits of the input boundary along the Earth-Sun line and the noon-midnight plane. Starting from this initial condition, the

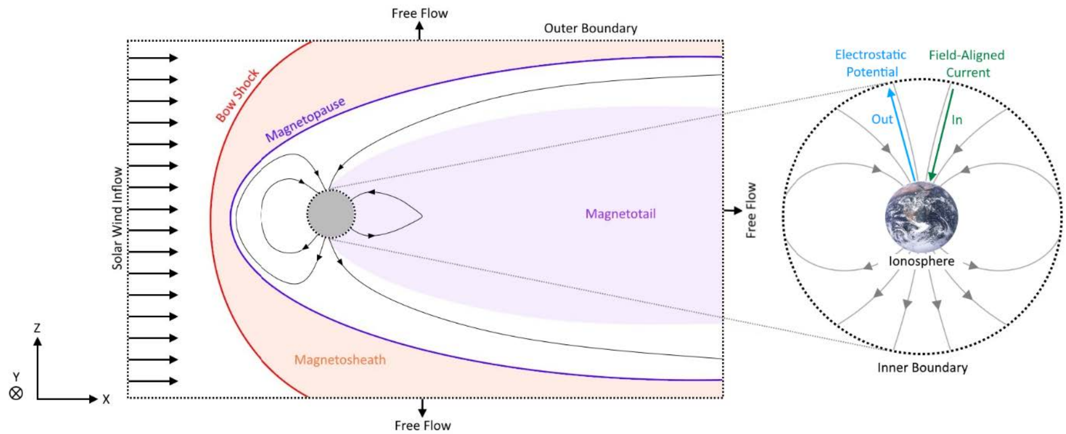

Figure 2. The simulation domain setup in Gorgon-Space.

magnetosphere's structure is dynamically reshaped by interactions with the CME-driven solar wind as the simulation progresses.

As indicated in the velocity panel of Fig. 3, the y and z components of the solar wind velocity are close to zero. This means that the solar wind reaching Earth has only the x-component of velocity, directed ~~along~~ along the Sun-Earth line. The decrease in particle density and the temperature rise, as shown in Fig. 3, may be associated with the formation of the bow shock. ~~The passage of plasma through the bow shock leads to a sudden drop in density (due to the slowdown) and an increase in particle temperature (due to the conversion of bulk kinetic energy to thermal energy). The observed changes in density and temperature in Fig. 3, signify this shock crossing. These changes serve as key indicators of the arrival of the pressure front at the magnetospheric boundary and the onset of energy transfer. These changes serve as key indicators of the arrival of the pressure front at the magnetospheric boundary and the onset of energy transfer. The consequences of this energy transfer for magnetospheric dynamics and subsequent ionospheric effects will be discussed.~~ The passage of plasma through the bow shock leads to a sudden drop in density (due to the slowdown) and an increase in particle temperature (due to the conversion of bulk kinetic energy to thermal energy). The observed changes in density and temperature in Fig. 3, signify this shock crossing. These changes serve as key indicators of the pressure front's arrival at the magnetospheric boundary and the onset of energy transfer. These changes serve as key indicators of the pressure front's arrival at the magnetospheric boundary and the onset of energy transfer. The consequences of this energy transfer for magnetospheric dynamics and subsequent ionospheric effects will be discussed.

The pronounced tailward stretching and distortion of the magnetotail observed in the XY plane during the CME1 impact (Fig. 4 c–d) are consistent with the onset of magnetic reconnection in the magnetotail. Under enhanced solar wind dynamic pressure and southward IMF conditions (often associated with strong CMEs), reconnection in the near-Earth plasma sheet can lead to the formation of X-lines and the ejection of plasmoids, resulting in the observed elongation and structural deformation of the tail (e.g., Baker et al., (1996); Hesse et al., (2004); Angelopoulos et al., (2008)). This

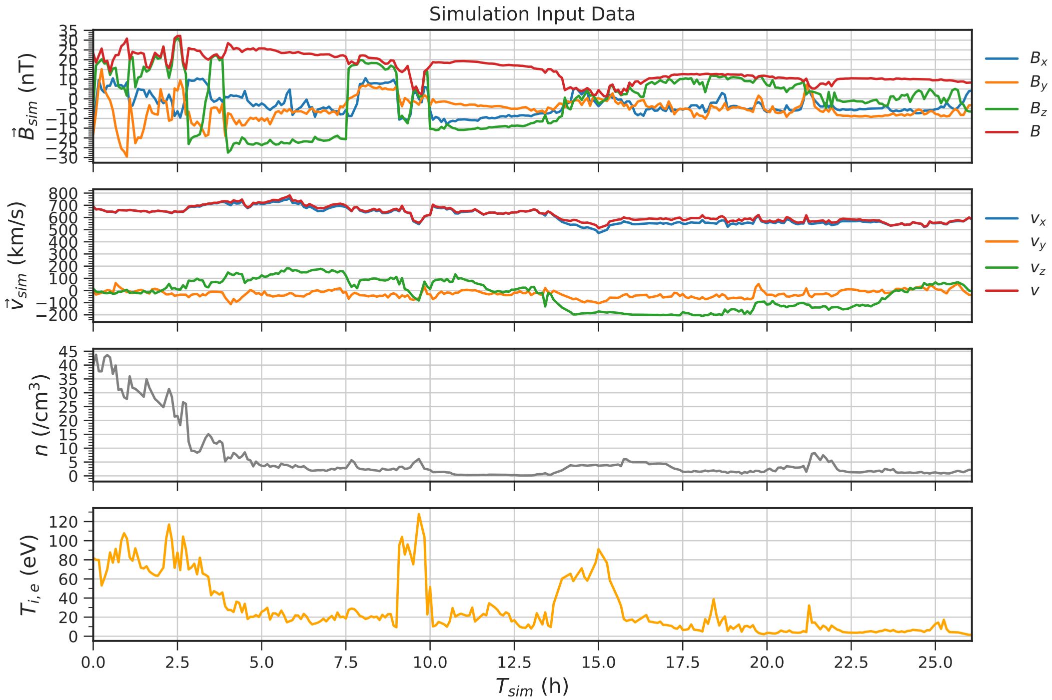

(a)

Figure 3. Upstream solar wind boundary conditions for the magnetospheric simulation. Time series of the solar wind parameters used as the initial and driving input for the Gorgon-Space MHD simulation, derived from the EUHFORIA heliospheric model. The data ~~corresponds~~ correspond to ~~the~~ conditions at the Earth-Sun L1 point for the period beginning at 00:03 UT on June 23, 2015, ~~coinciding~~ which coincides with the arrival of the first CME. From top to bottom, the panels show: the three vector components of the magnetic field B (in nT) and plasma velocity V (in km/s), the plasma density (in cm^{-3}), and the plasma temperature T (in eV). All vector components are presented in the Geocentric Solar Ecliptic (GSE) coordinate system.

process efficiently converts magnetic energy into kinetic and thermal energy, contributing to the global restructuring of the magnetosphere during geomagnetic storms. While reconnection also occurs at the dayside magnetopause, the tail configuration shown here is particularly indicative of nightside reconnection dynamics triggered by the intense solar wind forcing.

~~Fig.~~Figure 4 illustrates the evolution of thermal pressure and magnetic field topology during the arrival of CME1, as simulated by our global MHD model. The black lines represent magnetic field lines traced from seed points on a spherical surface at $r = 1R_E$, covering latitudes from -80° to +80° and longitudes spaced every 15°. Field lines are numerically integrated along the magnetic field vector until they either close within the magnetosphere (connecting back to the opposite hemisphere) or extend beyond the magnetopause into the solar wind (defined as open if they reach $x > 10R_E$ in the tail). The use of both X–Z (noon–midnight meridian) and X–Y (equatorial) planes allows us to reconstruct

the magnetosphere's three-dimensional response ~~of the magnetosphere~~ to CME1, revealing dayside compression, tail stretching, and topological signatures of magnetic reconnection.

Panel (a) depicts the magnetospheric state approximately two days before CME1 arrival, corresponding to the time of the CME's initiation at the Sun (June 21, 2015, 08:04 UT). While this snapshot provides context for the initial solar event, it does not represent the magnetospheric configuration immediately preceding the CME's impact at Earth. Panel (b), captured at 00:03 UT on June 23, 2015, depicts the magnetosphere at the time of CME1 arrival, showing significant dayside compression and elevated thermal pressure throughout the magnetosphere, particularly in the equatorial plane (X-Y). This pressure enhancement coincides with a dramatic reconfiguration of the magnetic topology, most notably, the pronounced tailward stretching and distortion of the magnetotail observed in the X-Y plane (Panels c–d).

In Fig. 4, reconnection sites are inferred from topological changes in field line connectivity and ~~localized~~ localised enhancements in thermal pressure gradients. Dayside reconnection is inferred near the subsolar magnetopause, around (~~$x \approx 10\breve{}12R_E, z \approx 0$~~$x \approx 10 - 12R_E, z \approx 0$) in the X-Z plane, where closed field lines abruptly transition to open ones. Nightside reconnection is inferred in the near-Earth plasma sheet of the magnetotail, approximately at (~~$x \approx \breve{}20to\breve{}25RE, y \approx 0$~~$x \approx$ to $-25\ R_E$, $y \approx 0$) in the ~~X-Y~~ $X - Y$ plane, where the stretched tail field lines exhibit a sharp reversal in direction and enhanced pressure, consistent with the formation of a neutral X-line and plasmoid ejection.

This tail deformation is consistent with the onset of magnetic reconnection in the near-Earth plasma sheet. Under the enhanced solar wind dynamic pressure and likely southward IMF conditions associated with CME1, reconnection can lead to the formation of X-lines and the ejection of plasmoids, resulting in the observed elongation and structural disruption of the tail Baker et al., (1996); Hesse et al., (2004); Angelopoulos et al., (2008). This process efficiently converts magnetic energy into kinetic and thermal energy, contributing to the global restructuring of the magnetosphere during geomagnetic storms. While reconnection also occurs at the dayside magnetopause, the topological changes in the tail, including increased open flux and the development of a stretched, asymmetric configuration, are particularly indicative of nightside reconnection dynamics triggered by the intense solar wind forcing.

Accurate prediction of CME arrival times must account for such magnetospheric shielding and internal reconfiguration effects; neglecting them can lead to overestimation of direct solar wind coupling and ~~mischaracterization~~ mischaracterisation of the geomagnetic response.

The dynamic pressure and magnetic topology during the CME2 impact are shown in Fig. 5. A comparison with the pre-CME state in Fig. 4 reveals the extreme compression caused by CME1. The magnetopause and bow shock are pushed inward by approximately $X/R_E \sim 10$, whereas on the dayside, it is around -20 for CME2. The magnetosphere continues to deflect ~~the majority~~ most of the solar wind~~flow~~, thereby shielding the inner region, albeit within a significantly reduced and deformed volume. In other words, the MHD simulations reveal a stark contrast in magnetospheric response between the strong CME1 and the weak CME2. The arrival of CME1 (Fig. 4) induces a severe compression of the dayside magnetopause and a significant enhancement of solar wind pressure across the entire magnetosphere, leading to a highly distorted, elongated tail structure. In contrast, the weaker CME2 (Fig. 5) produces only a moderate compression of the magnetopause and a much less pronounced pressure increase, resulting in a magnetospheric

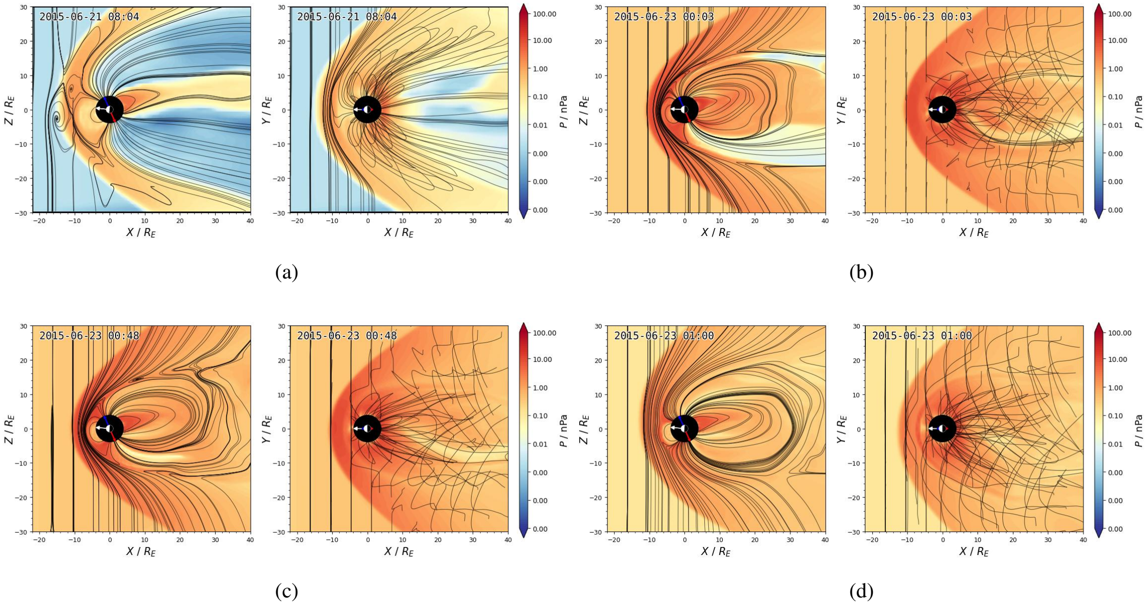

Figure 4. Snapshot of solar wind pressure from the MHD simulation with Gorgon-Space. It depicts the arrival time of the first CME, which ~~started~~ began on 21 June 2015 at 08:02 and ~~arrived at~~ reached Earth on 23 June 2015 at 00:03 UT, in the noon-midnight plane.

configuration that remains closer to its nominal state with a less perturbed tail. This demonstrates a direct correlation between CME intensity and the degree of global magnetospheric deformation and pressure loading.

~~Fig.~~Figure 6 depicts the changes in velocity caused by the CME1 at the magnetosphere. The first panel of Fig. 6 shows that the speed at the time of CME1 happening on the Sun is not noteworthy. Additionally, the magnetospheric magnetic field has a consistent shape and can fulfil its primary role as a protective barrier. Panels (b) to (d) depict the wind speed and magnetic configuration of the magnetosphere upon the arrival of CME1 at Earth. Upon initial observation, these three panels represent a notable degree of speed and an irregular magnetic structure resulting from the interaction between the solar wind and the magnetosphere. One can infer that energy from the solar wind is transferred to the Earth's magnetosphere via magnetic reconnection. This occurs when the interplanetary magnetic field connects ~~with~~ to the Earth's magnetic field at the magnetopause on the ~~dayside of the planet.~~ planet's dayside.

~~Fig.~~Figure 7 depicts the solar wind velocity and magnetic field configuration upon the arrival of CME2 at Earth. CME2 does not lead to high plasma velocity in the magnetosphere. Besides, in Fig. 7, in the $X-Z$ plane, the closed field regions get larger on the nightside, which could be due to a reduction in open flux content in the magnetosphere. This might lead to ~~a decrease in~~ decreased geomagnetic activity and smaller polar caps in the ionosphere.

The rate of magnetic reconnection and the amount of energy transferred are influenced by the ~~speed of the solar wind , the strength of the magnetic field , and its~~ solar wind speed, magnetic field strength, and orientation. Subsequently,

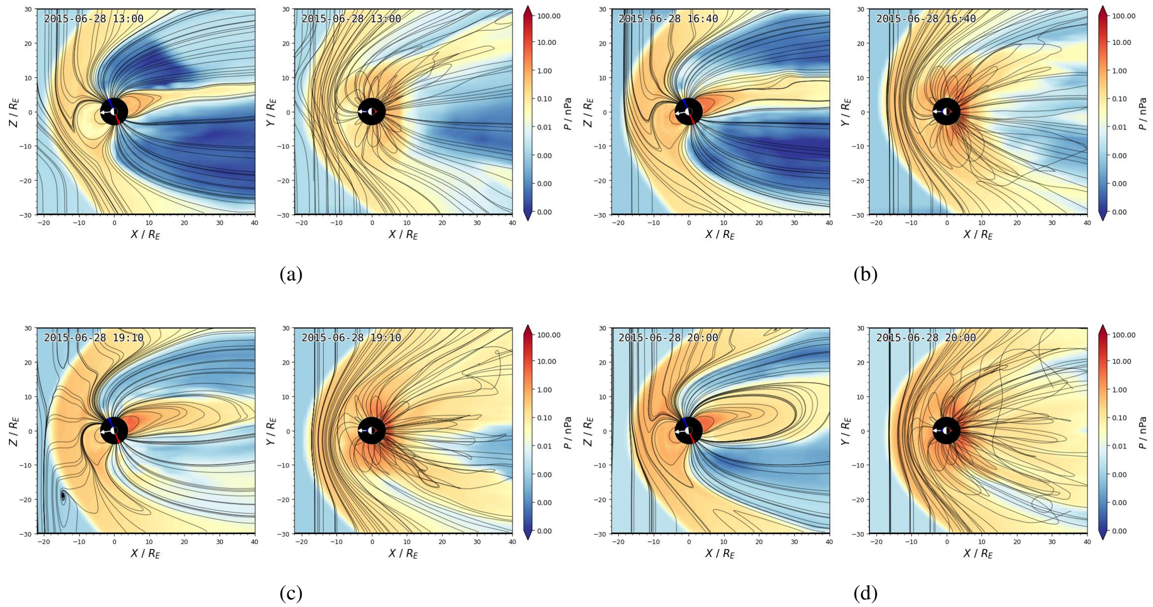

Figure 5. Snapshot of solar wind pressure from the MHD simulation with Gorgon-Space. It depicts the arrival time of the second CME, which ~~started~~ began on 25 June 2015 at 14:53 and ~~arrived at~~ reached Earth on 28 June 2015 at 12:52 UT, in the noon-midnight plane.

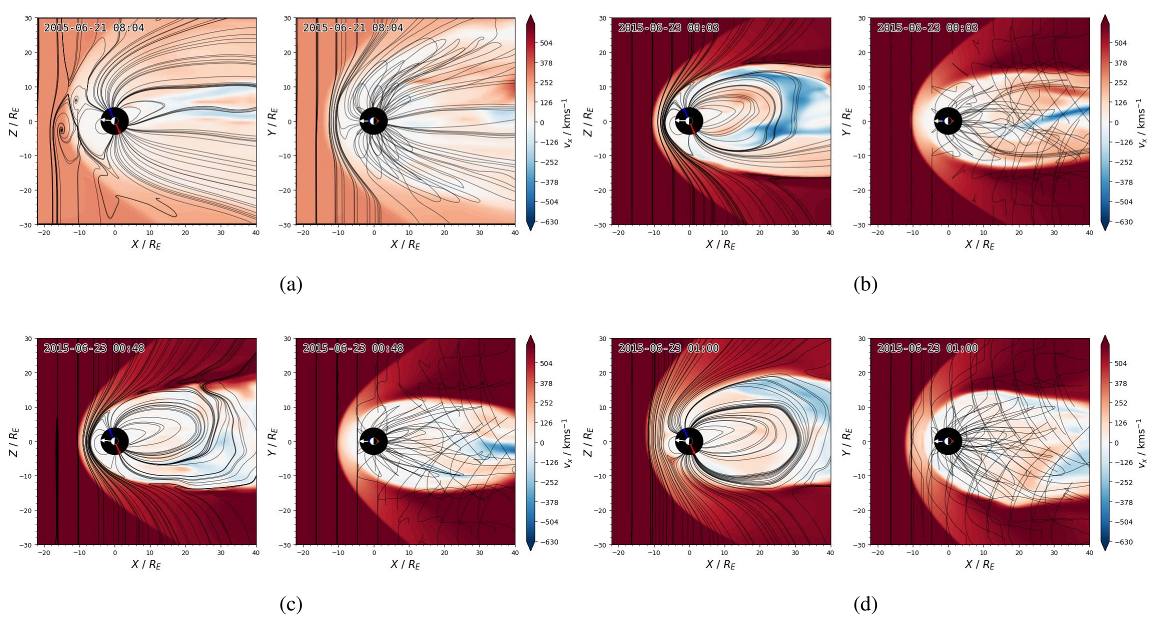

Figure 6. Snapshot of solar wind velocity from the MHD simulation with Gorgon-Space. It depicts the arrival time of the first CME, which ~~started~~ began on 21 June 2015 at 08:02 and ~~arrived at~~ reached Earth on 23 June 2015 at 00:03 UT, in the noon-midnight plane.

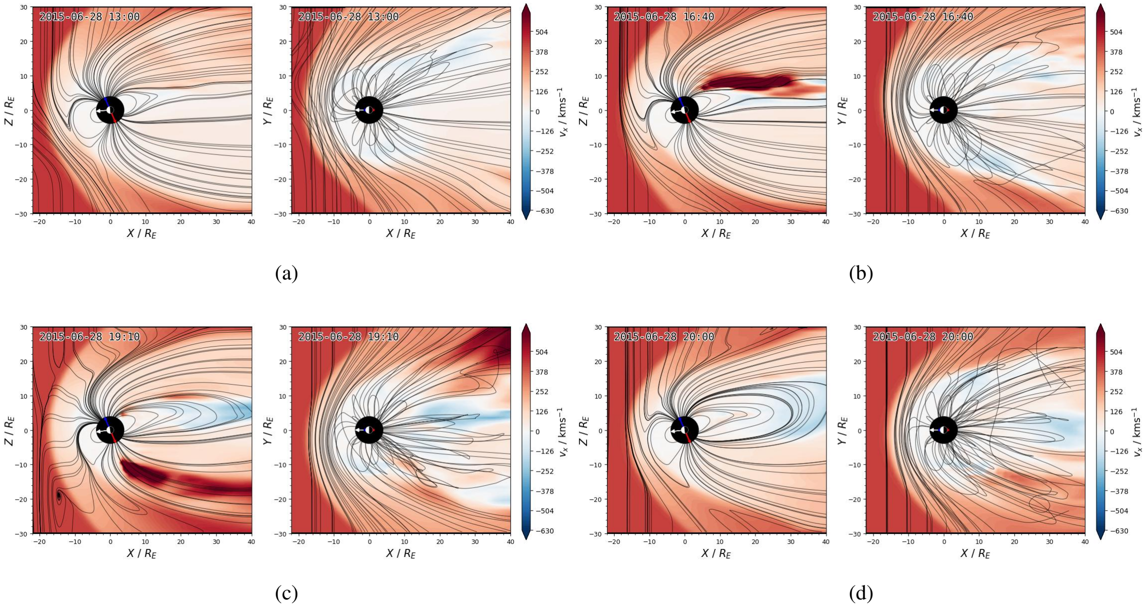

Figure 7. Snapshot of solar wind velocity from the MHD simulation with Gorgon-Space. It depicts the arrival time of the second CME, which ~~started~~ began on 25 June 2015 at 14:52 and ~~arrived at~~ reached Earth on 28 June 2015 at 12:52 UT, in the noon-midnight plane.

it was discovered that CME1 triggers a significant tempest on Earth and is accompanied by changes in the magnetic arrangement, increased speed and pressure of the solar wind enveloping the Earth, as previously anticipated in Fig. 1.

~~Fig.~~ Figure **5 showcases the changes in pressure and magnetic field in the vicinity of the Earth upon the arrival of CME2. As it was also shown in Fig. 1, there was no indication of a significant magnetic storm at the time when CME2 arrived. It can shed light on the impact of the background solar wind, which is the same in both CMEs, and thus it is not the primary factor in causing magnetic storms. Hence, it can be deduced that the nature of the CME and its interaction with other CMEs are crucial factors in determining the geomagnetic impact of CMEs interacting with the Earth.**

The transfer of energy from the solar wind into the Earth's magnetosphere–ionosphere system during geomagnetic storms is primarily governed by dayside magnetic reconnection, a process whose efficiency is controlled by the orientation and magnitude of the interplanetary magnetic field (IMF) and the solar wind speed. The southward component of the IMF ($Bz < 0$ in GSM coordinates) enables the solar wind magnetic field to reconnect antiparallel to Earth's northward-directed dayside field, thereby opening previously closed magnetospheric field lines and allowing solar wind momentum and energy to enter the system. The reconnection electric field, defined as E_y, serves as a widely accepted proxy for the rate of this energy transfer (e.g., Dungey, (1961); Gonzalez et al., (1994)).

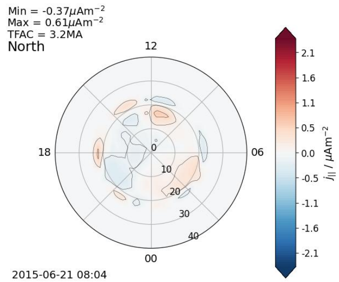

(a)

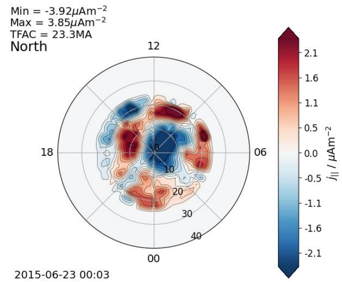

(b)

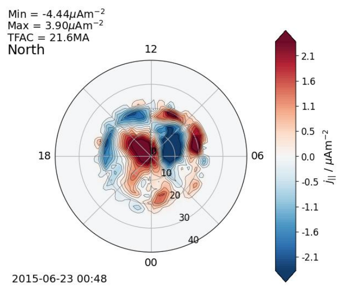

(c)

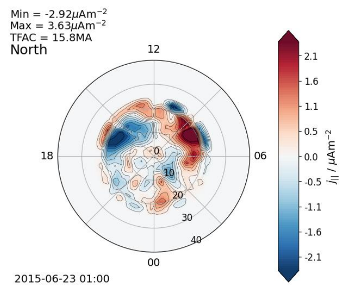

(d)

Figure 8. Snapshot of the ionospheric field-aligned current density in the Northern Hemisphere.

Figure 10 quantifies these key drivers during the June 2015 storm period. CME1, arriving on June 23, is characterized by an intense and sustained southward IMF (Bz ≈ –20 nT) that persists for several hours (Fig. 10 panel b). This drives a large reconnection electric field exceeding 15 mV/m (Fig. 10panel a), indicative of vigorous dayside reconnection. This enhanced energy input directly explains the observed magnetospheric compression, tail stretching, and nightside plasmoid formation (Fig. 4), as well as the intense field-aligned currents (Fig. 8) and elevated cross-polar cap potential of 160 kV (Fig. 11). These are all hallmarks of a strong substorm and storm-time convection driven by efficient solar wind–magnetosphere coupling.

In contrast, CME2, arriving on June 28, exhibits only brief and weak southward IMF excursions (~~$Bz > ˘5$~~ $Bz \geq -5$ nT for most of the event) and a correspondingly low Ey (~~< 3~~ ≤ 3 mV/m). This minimal reconnection activity results in negligible energy transfer, consistent with the absence of significant magnetospheric distortion (Fig. 5), weak FACs (Fig. 9), and low ionospheric convection potential (Fig. 12). Despite its high speed (Table 1), CME2 lacked the critical southward magnetic field component necessary for geoeffectiveness.

Thus, Fig. 10 provides the causal link between interplanetary conditions and the divergent magnetospheric–ionospheric responses to the two CMEs. It confirms that CME speed alone is insufficient to predict storm intensity; rather, the IMF Bz orientation and the resulting reconnection-driven energy coupling are the dominant factors. This observation

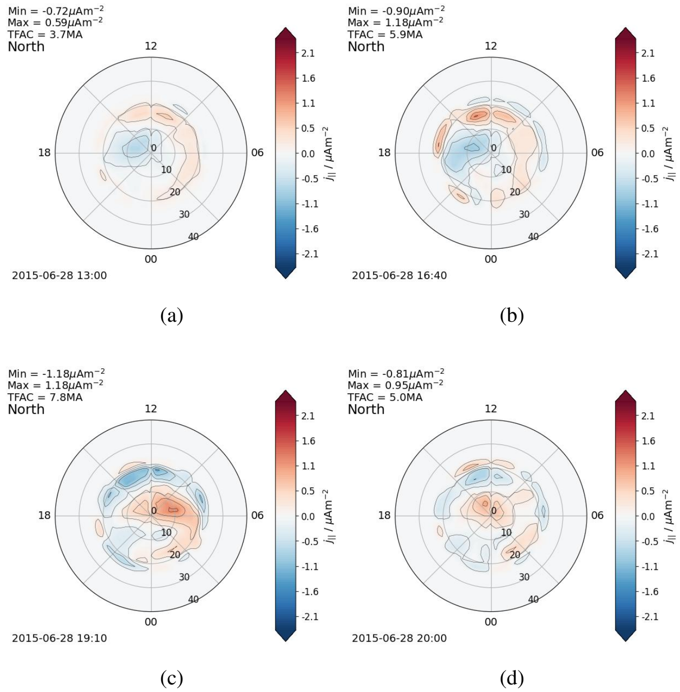

Figure 9. Snapshot of the ionospheric field-aligned current density in the Northern Hemisphere due to the interaction of the CME2.

validates a core principle of space-weather physics and underscores the importance of accurate IMF forecasting for predicting geomagnetic impacts.

3.1.2 Ionospheric Response

To model magnetosphere–ionosphere (M–I) coupling, Gorgon-Space employs a separate, height-integrated ionospheric module. The 3D MHD domain does not resolve the ionosphere; instead, its inner boundary is placed at $R_{\rm IB} = 4\,R_E$, where field-aligned currents (FACs) are computed from the magnetospheric solution via Ampère's law, $\mathbf{J}_{\parallel} = (\mathbf{J}\cdot\mathrm{b})\mathrm{b}$, with $\mathrm{b} = \mathrm{B}/|\mathrm{B}|$. These FACs are mapped along dipole magnetic field lines onto a 2D spherical ionospheric grid ~~located~~ at an effective altitude of ∼110 km—~~representing~~ corresponding to the E-region (90–150 km), where Hall and Pedersen conductivities peak.

Within the thin-shell approximation, the height-integrated ionospheric current is governed by Ohm's law: $\mathbf{J}_{\perp} = \Sigma_P\mathbf{E} + \Sigma_H(\mathrm{b}\times\mathbf{E})$, where Σ_P and Σ_H are the Pedersen and Hall conductances. In this study, these conductances are calculated using empirical relations: a solar EUV-driven background (with square-root dependence on solar flux) and an auroral component derived from magnetospheric electron energy flux mapped along field lines. The electrostatic potential ϕ is obtained by solving the 2D current continuity equation $\nabla_{\perp}\cdot\mathbf{J}_{\perp} = -\nabla_{\perp}\cdot(\Sigma_P\nabla_{\perp}\phi) = J_{\parallel}$, ensuring current

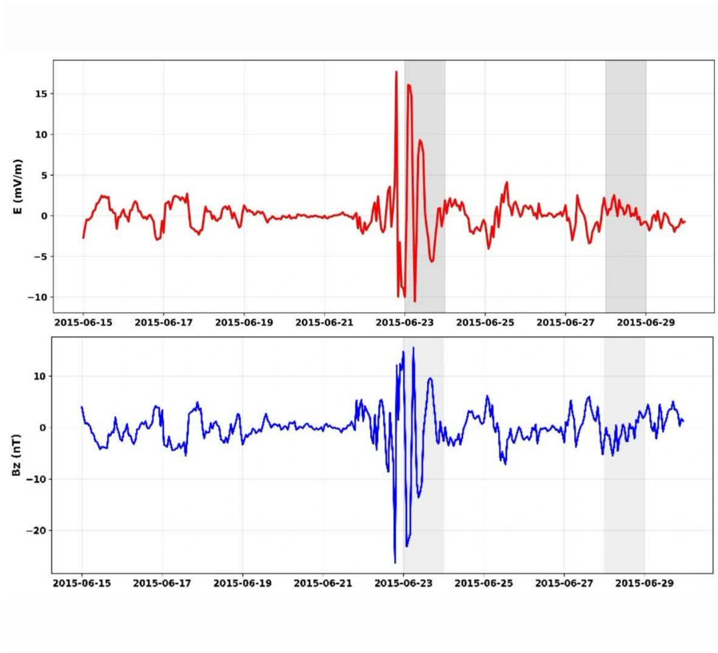

(a)

Figure 10. Time series of (a) the reconnection electric field Ey (in mV/m) during June 15–29, 2015 and (b) the Bz component of the interplanetary magnetic field (IMF). The ~~gray-shaded~~ grey-shaded intervals highlight periods of enhanced geomagnetic activity associated with the arrival of CME1 (June 23) and CME2 (June 28). Strongly negative Bz and elevated Ey values indicate favourable conditions for efficient magnetic reconnection at the dayside magnetopause, thereby facilitating direct transfer of solar wind energy ~~transfer~~ into the magnetosphere.

closure. The resulting potential distribution is mapped back along the dipole field lines to the MHD inner boundary, thereby providing a self-consistent time-dependent boundary condition for the plasma flow.

This coupling enables energy and momentum transfer across the system: FACs generated in the magnetosphere (where $\nabla \times \mathrm{B} \neq 0$) flow into the ionosphere, ~~closing via~~ where they are closed by perpendicular Pedersen and Hall currents. The resulting Lorentz force, $\mathrm{J}_{\perp} \times \mathrm{B}$, drives ionospheric plasma convection and, through ion–neutral collisions, neutral winds. This convection pattern, anchored by FAC stress, transports magnetic flux tubes globally, thereby mediating the large-scale M–I energy exchange that underpins space-weather impacts.

$$j_{\parallel} = \frac{(\mathbf{j} \cdot \mathbf{B})\mathbf{B}}{|\mathbf{B}|^2},$$

The accumulation of current density aligned with the magnetic field can be attributed to the interaction between the solar wind and the magnetosphere. The predominant energy transfer and current alignment in the ionosphere were driven primarily by the boundary conditions. To accurately predict space weather, it is necessary to have a solid under-

standing of the physics underlying these coupling processes. Determining the accuracy of MHD codes in reproducing ~~the electric fields in the plasma sheet when the solar wind interacts with the magnetosphere~~ plasma sheet electric fields during solar wind-magnetosphere interactions is of utmost significance for Space Weather applications.

~~Fig.~~Figure 8 presents the evolution of field-aligned current (FAC) density in the Northern Hemisphere ionosphere in response to the sudden commencement (SC) driven by the arrival of CME1 at Earth, capturing the onset, peak, and initial recovery of the disturbance. Panel (a) shows the quiet-time pre-impact baseline at 08:02 UT on June 21. Following the SC, Panels (b) and (c) depict the development and peak of the intense electrodynamic response. Panel (b), immediately after the SC at 00:03 UT on June 23, reveals a localized, dayside-enhanced FAC pattern. This initial enhancement is consistent with the characteristic Preliminary Impulse (PI) observed during shock-induced compressions, often attributed to the compression of the dayside magnetosphere and the associated Chapman-Ferraro (CFAC) currents (e.g.,Araki, (1994)). Panel (c) represents the peak intensity, showing a substantial increase in total current magnitude to approximately 23 MA and a poleward shift of the primary current regions. This stronger, poleward-expanding structure corresponds to the Main Impulse (MI). The MI signifies the full engagement of the global substorm current system (R1 FACs), which is directly driven by the large-scale magnetospheric convection electric field. This convection electric field ($E_{conv} = -v \times B$) is itself established by enhanced dayside magnetic reconnection under the prolonged southward IMF conditions in the CME sheath. Panel (d) shows the start of the recovery phase in the Northern Hemisphere, where the current density magnitude decreases, and the pattern has shifted poleward from a colatitude of 0° to a range of 10°–20°. The clear temporal sequence from quiet conditions (a) through the distinct PI and MI phases (b, c) and into recovery (d) demonstrates that the Gorgon-Space code captures the fundamental two-phase ionospheric electrodynamic response to a CME-driven shock, a key benchmark for validating space-weather models. The intense MI-phase FACs are a primary conduit for energy transfer from the magnetosphere, underscoring their critical role in driving space-weather effects such as geomagnetically induced currents Pulkkinen, (2007); Pirjola, (2005).

~~Fig.~~Figure 9 demonstrates that CME2, despite a higher arrival speed, did not generate a significant ionospheric FAC response compared to CME1. This indicates that CME speed alone is not a reliable predictor of geoeffectiveness. The stronger response to CME1 may be related to other factors, such as the orientation of its embedded magnetic field or the conditions of the preceding solar wind and CME-CME interactions Sabri & Poedts, (2025).

The Fig. 11 shows the electric potential response in the ionosphere. The illustration shows the cross-polar cap electric potential (CPCP) in the ionosphere, which is widely used to assess the worldwide convection intensity. This shows the disparities between the highest and lowest electric potential values in the ionosphere. CPCP was initially derived from the integral rate of dayside-merging and can be used as an estimate of the key parameter of dayside-merging, as in (Gordeev et al., (2015)).

The first panel in Fig. 11 shows the level of the electric potential in the ionosphere at the onset of the initial coronal mass ejection (CME1). Panel (b) of Fig. 11 displays the ionospheric electric potential reaction during the initial arrival of the first coronal mass ejection (CME1) at the Earth. Comparing ~~both~~ the two panels helps ~~to~~ determine the impact

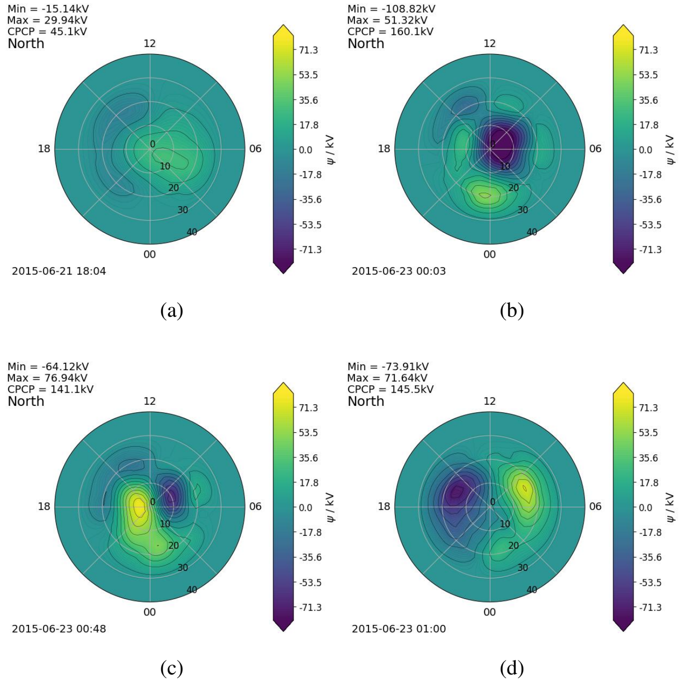

Figure 11. Ionospheric response electric potential during the happening of the first CME and its arriving at the Earth. Yellow indicates the positive ~~**potential**~~potential, and blue means negative **potential**.

of the solar wind on Earth, ~~specifically resulting in~~ yielding an ionospheric electric potential ~~value~~ of approximately 160 kV ~~in the ionosphere~~ during the CME1 impact. This elevated cross-polar cap potential (∼160 kV) is a direct measure of the strength of the magnetospheric convection electric field. This same convection electric field, when mapped back along magnetic field lines into the magnetosphere, drives the bulk plasma motion via the $E \times B$ drift. Consequently, the weak ionospheric potential during CME2 (Fig. 12) is physically consistent with the low plasma velocities observed in the magnetosphere for that event (Figs. 6, 7). ~~Fig.~~Figure 12 illustrates the electric potential in the ionosphere when CME2 reaches the Earth. As predicted, the arrival of CME2 at Earth does not cause any notable electric potential in the ionosphere. The elevated ionospheric potential (∼160 kV) is a signature of a strong magnetospheric convection electric field. This large-scale field governs the global transport and ~~energization~~ energisation of plasma. While the quasi-static ionospheric field itself does not directly accelerate particles to high energies, the associated magnetospheric convection can inject plasma-sheet particles into the inner magnetosphere, where they may subsequently be accelerated to ring-current and radiation-belt energies by processes such as radial diffusion and wave-particle interactions.

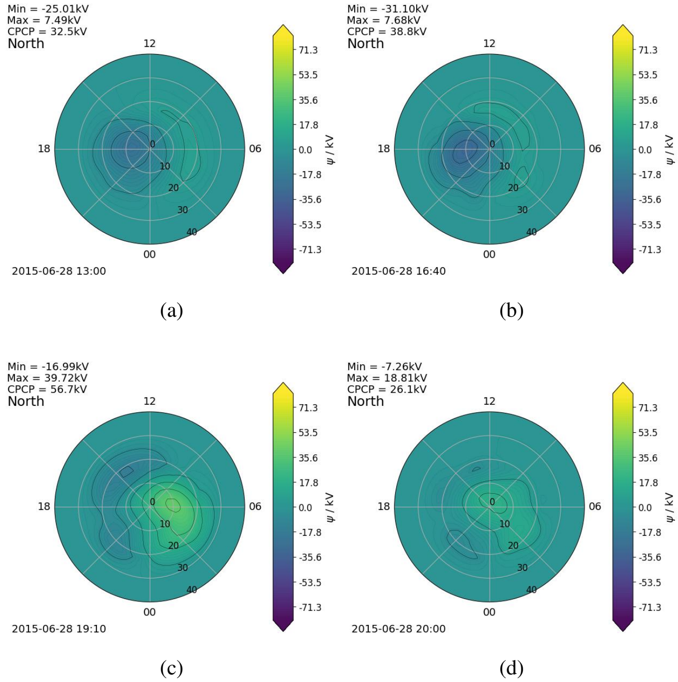

Figure 12. Ionospheric response electric potential during the arrival of CME2 at Earth. Yellow indicates the positive ~~potential~~potential, and blue means negative ~~potential~~potential.

4 Conclusions

Because of their profound impacts on both scientific understanding and technological systems, coronal mass ejections (CMEs) remain a central focus of space weather research. CMEs drive intense geomagnetic storms, capable of enhancing radiation belt fluxes that threaten satellites, and can produce solar energetic particles (SEPs) that disrupt spacecraft operations and aviation safety. Understanding how CME properties, such as speed, magnetic structure, and interaction with the ambient solar wind or other CMEs, determine their geoeffectiveness is therefore critical.

In this study, we examined two CMEs that impacted Earth on June 23 and June 28, 2015 (identified as CME1 and CME2 in Sabri & Poedts, (2025)), which exhibited markedly different geoeffectiveness despite both being fast events. Using an end-to-end modelling chain that couples the EUHFORIA heliospheric model to the Gorgon-Space global MHD code, we performed time-dependent, 3D simulations of the resulting magnetospheric and ionospheric responses.

Our key findings are as follows:

1. **CME1 induced firm compression of the dayside magnetosphere and pronounced tailward stretching in the XY plane, consistent with enhanced magnetic reconnection under sustained southward IMF conditions. This led to significant deformation of the bow shock and magnetopause boundaries.**

2. CME1 triggered a major geomagnetic storm, ~~characterized~~ characterised by a total field-aligned current (FAC) of approximately 23 MA concentrated in the Northern Hemisphere ionosphere, reflecting intense energy deposition from the magnetosphere.

3. The geoeffectiveness of a CME is not determined by its launch speed alone. Although CME2 was faster than CME1, it produced only a weak response due to the absence of prolonged southward IMF, underscoring that interplanetary magnetic field orientation, not CME kinematics, governs storm intensity.

4. The ionospheric cross-polar cap potential (CPCP) reached $\sim$160 kV during CME1, consistent with strong convection driven by dayside reconnection. This electric potential facilitates the transport of plasma-sheet particles toward Earth, thereby supporting ring-current growth and auroral precipitation.

5. The ~~strong temporal correlation between EUHFORIA'~~close temporal correspondence between EUHFORIA's predicted solar wind conditions at L1 and the magnetospheric–ionospheric response simulated by Gorgon-Space~~(e.g., timing of compression, FAC~~ —evident in the accurately reproduced timing of magnetopause compression, field-aligned current intensification, and cross-polar cap potential ~~) demonstrates the~~ evolution—demonstrates that our coupled modeling system captures the expected causal chain of solar wind–magnetosphere coupling. This agreement validates the self-consistency and predictive capability of ~~our coupled modelling approach.~~

   the EUHFORIA–Gorgon-Space framework.

This work makes three distinct contributions to space weather forecasting:

1. Operational validation: We demonstrate the first end-to-end EUHFORIA$\longrightarrow$Gorgon-Space chain that accurately forecasts magnetospheric drivers (FACs >23 MA, CPCP 160 kV) from heliospheric CME parameters, a critical capability for predicting GIC risks to power grids.

2. Physics-based discrimination: By resolving the CME1/CME2 contrast, we provide observational proof that IMF orientation (not speed) controls storm intensity — enabling forecasters to reject false alarms from fast CMEs with unfavourable magnetic geometry.

3. Numerical robustness: Gorgon-Space's $\nabla \cdot \mathbb{B} = 0$-preserving formulation captures extreme magnetospheric compression during CME impacts without numerical instabilities — a prerequisite for reliable operational forecasting during extreme events. While global MHD models have simulated storm-time magnetospheres for decades, this study provides the first quantitative validation of field-aligned current intensities (>23 MA) during the initial compression phase of a G4 storm using a $\nabla \cdot$B=0-preserving code. This capability is critical for operational GIC forecasting, as FACs directly drive geomagnetically induced currents in power grids — a risk quantified here through direct coupling to ionospheric potentials (160 kV) rather than proxy indices alone. Unlike previous end-to-end modeling studies that stop at magnetospheric boundaries, our EUHFORIA-Gorgon-Space chain quantifies the complete energy pathway from heliospheric CME parameters to ionospheric electrodynamic impacts (FACs, convection

potentials). This bridges a critical gap in operational space-weather forecasting by translating L1 solar wind measurements into actionable GIC risk assessments for power grid operators.

This work demonstrates that Gorgon-Space, with its divergence-free magnetic-field formulation and validated ionosphere coupling, provides a robust platform for translating heliospheric CME forecasts into quantifiable space-weather impacts in near-Earth space. While global MHD models such as SWMF and OpenGGCM have successfully simulated storm-time magnetospheres, few studies have examined the transient, high-fidelity evolution of field-aligned currents during the initial compression and main phase of CME-driven storms using a $\nabla \cdot \mathbb{B} = 0$-preserving code. Gorgon-Space's vector-potential formulation provides numerical stability during extreme compressions, enabling accurate capture of FAC dynamics that drive geomagnetically induced currents (GICs). This study demonstrates the first application of the EUHFORIA–Gorgon-Space chain to resolve the complete sequence from CME launch to the ionospheric electrodynamic response, offering a validated framework for operational space-weather forecasting.

Code and data availability. We used the EUHFORIA code to conduct a numerical study, which is publicly available via the VSWMC at https://euhforia.com/. Additionally, we used the Gorgon Space code to simulate the effects of CMEs on Earth.

Author contributions. Authors have contributed to writing the manuscript.

Competing interests. The contributor author has declared that none of the authors has any competing interest.

Acknowledgements. SP is funded by the European Union (ERC, Open SESAME, 101141362). Views and opinions expressed are, however, those of the author(s) only and do not necessarily reflect those of the European Union or the European Research Council. Neither the European Union nor the granting authority can be held responsible for them.

These results were also obtained in the framework of the projects C16/24/010 (C1 project Internal Funds KU Leuven), G0B5823N and G002523N (WEAVE) (FWO-Vlaanderen), and 4000145223 (SIDC Data Exploitation (SIDEX2), ESA Prodex). For the computations, we used the infrastructure of the VSC-Flemish Supercomputer Centre, funded by the Hercules Foundation and the Flemish Government, Department of EWI.

References

Angelopoulos, V., McFadden, J. P., Larson, D., et al. 2008, Science, 321, 931, https://doi.org/10.1126/science.1160495

Araki, T. 1994, in *Solar Wind Sources of Magnetospheric Ultra-Low-Frequency Waves*, Geophysical Monograph Series, Vol. 81 (Washington, DC: American Geophysical Union), 183, https://doi.org/10.1029/GM081p0183

Araki, T. 1974, J. Geophys. Res., 79, 3131, https://doi.org/10.1029/JA079i022p03131

Astafyeva, E., Yasyukevich, Y., Maksikov, A., & Zhivetiev, I. 2014, Space Weather, 12, 418, https://doi.org/10.1002/2014SW001072

Axford, W. I., & Hines, C. O. 1961, Canadian J. Phys., 39, 1433, https://doi.org/10.1139/p61-172

Baker, D. N., Pulkkinen, T. I., Angelopoulos, V., Baumjohann, W., & McPherron, R. L. 1996, J. Geophys. Res. Space Phys., 101, 12975, https://doi.org/10.1029/95JA03753

Bartels, J., & Veldkamp, J. 1950, J. Geophys. Res., 55, 214, https://doi.org/10.1029/JZ055i002p00214

Bartels, J., & Veldkamp, J. 1949, J. Geophys. Res., 54, 295, https://doi.org/10.1029/JZ054i003p00295

Benson, D. J. 1992, Comput. Methods Appl. Mech. Eng., 99, 235, https://doi.org/10.1016/0045-7825(92)90043-Q

Burgess, D., & Scholer, M. 2013, Space Sci. Rev., 178, 513, https://doi.org/10.1007/s11214-012-9958-7

Chittenden, J. P., Lebedev, S. V., Jennings, C. A., Bland, S. N., & Ciardi, A. 2004, Plasma Phys. Control. Fusion, 46, B457, https://doi.org/10.1088/0741-3335/46/12B/039

Ciardi, A., Lebedev, S. V., Frank, A., Blackman, E. G., Chittenden, J. P., Jennings, C. A., et al. 2007, Phys. Plasmas, 14, 056501, https://doi.org/10.1063/1.2723243

Demyanov, V. V., Yasyukevich, Yu. V., Ishin, A. B., & Astafyeva, E. I. 2012, GPS Solut., 16, 289, https://doi.org/10.1007/s10291-011-0232-8

Dryer, M. 1961, Planet. Space Sci., 6, 305, https://doi.org/10.1016/0032-0633(61)90021-7

Dryer, M., Merritt, D. L., & Aronson, P. M. 1967, J. Geophys. Res., 72, 2955, https://doi.org/10.1029/JZ072i011p02955

Dungey, J. W. 1961, Phys. Rev. Lett., 6, 47, https://doi.org/10.1103/PhysRevLett.6.47

Eastwood, J. P., Lucek, E. A., Mazelle, C., Meziane, K., Narita, Y., Pickett, J., & Treumann, R. A. 2005, Space Sci. Rev., 118, 41, https://doi.org/10.1007/s11214-005-3580-5

Eastwood, J. P., Hapgood, M. A., Biffis, E., Bentin, D., Bisi, M. M., & Green, L., et al. 2018, Space Weather, 16, 2052, https://doi.org/10.1029/2018SW001997

Eggington, J. W. B., Eastwood, J. P., Mejnertsen, L., Desai, R. T., & Chittenden, J. P. 2020, J. Geophys. Res. Space Phys., 125, e2019JA027510, https://doi.org/10.1029/2019JA027510

Gieseler, J., Dresing, N., Palmroos, C., von Forstner, J. L. F., & Veronig, A., et al. 2022, Front. Astron. Space Sci., 10, 1073389, https://doi.org/10.3389/fspas.2023.1073389

Gombosi, T. I., De Zeeuw, D. L., Ebihara, Y., et al. 2021, Space Weather, 19, e2021SW002818, https://doi.org/10.1029/2021SW002818

Gonzalez, W. D., Joselyn, J. A., Kamide, Y., Kroehl, H. W., Rostoker, G., Tsurutani, B. T., & Vasyliūnas, V. M. 1994, J. Geophys. Res. Space Phys., 99, 5771, https://doi.org/10.1029/93JA02867

Gordeev, E., Sergeev, V., Honkonen, I., & Wiltberger, M. 2015, Space Weather, 13, 868, https://doi.org/10.1002/2015SW001279

Gosling, J. T. 1993, J. Geophys. Res. Space Phys., 98, 18937, https://doi.org/10.1029/93JA01896

Grib, S. A., Brunelli, B. E., Dryer, M., & Shen, W. W. 1979, J. Geophys. Res., 84, 5907, https://doi.org/10.1029/JA084iA10p05907

Hayes, L. A., Gallagher, P. T., McCauley, J., Dennis, B. R., Ireland, J., & Inglis, A. 2017, J. Geophys. Res. Space Phys., 122, 10173, https://doi.org/10.1002/2017JA024570

Hesse, M., Birn, J., & Kuznetsova, M. 2004, J. Geophys. Res. Space Phys., 109, A11212, https://doi.org/10.1029/2004JA010558

Iyemori, T. 1990, Journal of Geomagnetism and Geoelectricity, 42, 473, https://doi.org/10.5636/jgg.42.473

Jennings, C. A., Cuneo, M. E., Waisman, E. M., Sinars, D. B., Ampleford, D. J., et al. 2010, Phys. Plasmas, 17, 092703, https://doi.org/10.1063/1.3483260

Jerab, M., Nemecek, Z., Safrankova, J., Jelinek, K., & Merka, J. 2005, Planet. Space Sci., 53, 85, https://doi.org/10.1016/j.pss.2004.09.030

Joselyn, J. A. 1990, J. Geophys. Res. Space Phys., 95, 7785, https://doi.org/10.1029/JA095iA06p07785

Kappenman, J. G. 2001, in IEEE/PES Transmission and Distribution Conference and Exposition, Vol. 1, 251–256, https://doi.org/10.1109/TDC.2001.914859

Kumar, P., Nakariakov, V. M., Karpen, J. T., & Cho, K. S. 2024, Nat. Commun., 15, 2667, https://doi.org/10.1038/s41467-024-46980-9

Lavraud, B., & Rouillard, A. 2013, Proc. Int. Astron. Union, 8, 273, https://doi.org/10.1017/S1743921312023591

Lucek, E. A., Constantinescu, D., Goldstein, M. L., Pickett, J., et al. 2005, Space Sci. Rev., 118, 95, https://doi.org/10.1007/s11214-005-3072-8

Lugaz, N., Farrugia, C. J., Winslow, R. M., et al. 2016, J. Geophys. Res. Space Phys., 121, 10861, https://doi.org/10.1002/2016JA023300

Lyon, J. G. 2000, Science, 288, 2116, https://doi.org/10.1126/science.288.5473.2116

McLaughlin, J. A., Nakariakov, V. M., Dominique, M., Jelínek, P., & Takasao, S. 2018, Space Sci. Rev., 214, 45, https://doi.org/10.1007/s11214-018-0477-4

Mejnertsen, L., Eastwood, J. P., Hietala, H., Schwartz, S. J., & Chittenden, J. P. 2018, J. Geophys. Res. Space Phys., 123, 259, https://doi.org/10.1002/2017JA024764

Mejnertsen, L., Eastwood, J. P., Chittenden, J. P., & Masters, A. 2016, J. Geophys. Res. Space Phys., 121, 7497, https://doi.org/10.1002/2016JA022708

Merka, J., Szabo, A., Slavin, J. A., & Peredo, M. 2005, J. Geophys. Res., 110, A04202, https://doi.org/10.1029/2004JA010729

Moore, T. E., Peterson, W. K., Russell, C. T., Chandler, M. O., Collier, M. R., et al. 1999, Geophys. Res. Lett., 26, 2343, https://doi.org/10.1029/1999GL900495

Newell, P. T., Sotirelis, T., Liou, K., & Rich, F. J. 2008, J. Geophys. Res. Space Phys., 113, A04218, https://doi.org/10.1029/2007JA012845

Ogino, T. 1994, J. Geomag. Geoelectr., 46, 301, https://doi.org/10.5636/jgg.46.301

Pallocchia, G. 2013, J. Geophys. Res. Space Phys., 118, 331, https://doi.org/10.1029/2012JA018195

Peredo, M., Slavin, J. A., Mazur, E., & Curtis, S. A. 1995, J. Geophys. Res., 100, 7907, https://doi.org/10.1029/94JA03378

Pirjola, R. 2005, Adv. Space Res., 36, 2231, https://doi.org/10.1016/j.asr.2004.09.040

Pomoell, J., & Poedts, S. 2018, J. Space Weather Space Clim., 8, A35, https://doi.org/10.1051/swsc/2018020

Poedts, S., Kochanov, A., Lani, A., et al. 2020, J. Space Weather Space Clim., 10, 14, https://doi.org/10.1051/swsc/2020017

Prech, L., Nemecek, Z., & Safrankova, J. 2008, Geophys. Res. Lett., 35, L17S02, https://doi.org/10.1029/2008GL033851

Priyadarshi, S., Zhang, Q. H., Ma, Y. Z., Wang, Y., & Xing, Z. Y. 2016, J. Geophys. Res. Space Phys., 121, 5706, https://doi.org/10.1002/2015JA022182

Pulkkinen, T. 2007, Living Rev. Sol. Phys., 4, 1, https://doi.org/10.12942/lrsp-2007-1

Rama Rao, P. V. S., Gopi Krishna, S., Vara Prasad, J., Prasad, S. N. V. S., Prasad, D. S. V. V. D., & Niranjan, K. 2009, Ann. Geophys., 27, 2101, https://doi.org/10.5194/angeo-27-2101-2009

Raeder, J. 1995, Adv. Space Res., 16(6), 37, https://doi.org/10.1016/0273-1177(95)00318-P

Rodgers-Lee, D., et al. (2021). EUHFORIA predictions for the 10 September 2017 CME event. *Space Weather*, 19, e2020SW002694.

Sabri, S., Poedts, S., & Ebadi, H. 2019, A&A, 623, A81, https://doi.org/10.1051/0004-6361/201833797

Sabri, S., Ebadi, H., & Poedts, S. 2020, ApJ, 902, 11, https://doi.org/10.3847/1538-4357/abb45c

Sabri, S., Vasheghani Farahani, S., Ebadi, H., & Poedts, S. 2020, Sci. Rep., 10, 15603, https://doi.org/10.1038/s41598-020-72629-3

Sabri, S., Ebadi, H., & Poedts, S. 2021, ApJ, 922, 123, https://doi.org/10.3847/1538-4357/ac21d0

Sabri, S., Ebadi, H., & Poedts, S. 2021, ApJ, 924, 126, https://doi.org/10.3847/1538-4357/ac323d

Sabri, S., Ebadi, H., & Poedts, S. 2023, ApJ, 944, 72, https://doi.org/10.3847/1538-4357/aca76a

Sabri, S., & Poedts, S. 2025, Adv. Space Res., https://doi.org/10.1016/j.asr.2025.11.081

Samsonov, A. A., Sibeck, D. G., & Imber, J. 2010, J. Geophys. Res., 115, A05207, https://doi.org/10.1029/2009JA014696

Smith, R. A., Lazarus, J., Hohenberger, M., Marocchino, A., Robinson, J. S., et al. 2007, Plasma Phys. Control. Fusion, 49, B117, https://doi.org/10.1088/0741-3335/49/12B/S11

Sorathia, K. A., Wiltberger, M., Merkin, V. G., et al. 2022, Front. Astron. Space Sci., 9, 957411, https://doi.org/10.3389/fspas.2022.957411

Smith, A. W., Freeman, M. P., Rae, I. J., & Forsyth, C. 2019, Space Weather, 17, 1605, https://doi.org/10.1029/2019SW002257

Spreiter, J. R., Summers, A. L., & Alksne, A. Y. 1966, J. Geophys. Res., 71, 1, https://doi.org/10.1029/JZ071i001p00001

Sugiura, M. 1964, Annals of the International Geophysical Year, 35, 7

Wiltberger, M., Rigler, E. J., Merkin, V., & Lyon, J. G. 2017, J. Geophys. Res. Space Phys., 122, 7055, https://doi.org/10.1002/2017JA024082

Yagi, M., Seki, K., & Matsumoto, Y. 2009, J. Geophys. Res. Space Phys., 114, A12217, https://doi.org/10.1029/2009JA014236

Zheng, Y. 2013, Space Weather, 11, 641, https://doi.org/10.1002/2013SW000971